J. Fluid Mech. (2021), *vol*. 915, A60, doi:10.1017/jfm.2021.21

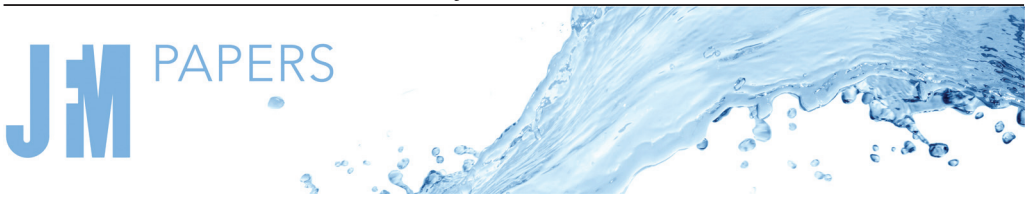

Effects of Prandtl number in quasi-two-dimensional Rayleigh–Bénard convection

Xiao-Ming Li[1,2], Ji-Dong He[1], Ye Tian[1,2], Peng Hao[1] and Shi-Di Huang[1,†]

[1]Center for Complex Flows and Soft Matter Research, and Department of Mechanics and Aerospace Engineering, Southern University of Science and Technology, Shenzhen 518055, PR China

[2]Guangdong Provincial Key Laboratory of Turbulence Research and Applications, Southern University of Science and Technology, Shenzhen 518055, PR China

(Received 3 September 2020; revised 16 November 2020; accepted 29 December 2020)

We report an experimental study of the Prandtl-number effects in quasi-two-dimensional (quasi-2-D) Rayleigh–Bénard convection. The experiments were conducted in four rectangular convection cells over the Prandtl-number range of $11.7 \leqslant Pr \leqslant 650.7$ and over the Rayleigh-number range of $6.0 \times 10^8 \leqslant Ra \leqslant 3.0 \times 10^{10}$. Flow visualization reveals that, as Pr increases from 11.7 to 145.7, thermal plumes pass through the central region much less frequently and their self-organized large-scale motion is more confined along the periphery of the convection cell. The large-scale flow is found to break down for higher Pr, resulting in a regime transition in the Reynolds number Re. For the Pr range with a large-scale flow of system size, the Re number, Nusselt number Nu and local temperature fluctuations were investigated systematically. It is found that Re scales as $Re \sim Ra^{0.58}Pr^{-0.82}$ in the present geometry, which suggests that it is in line with the behaviour in the 2-D configuration. On the other hand, the measured $Nu(Ra, Pr)$ relation $Nu \sim Ra^{0.289}Pr^{-0.02}$ tends to be compatible with the finding in a three-dimensional (3-D) system. For the temperature fluctuations in the cell centre and near the sidewall, they exhibit distinct Ra-dependent scalings that could not be accounted for with existing theories, but their Pr dependences for $Pr \lesssim 50$ are in agreement with the predictions by Grossmann & Lohse (*Phys. Fluids*, vol. 16, 2004, pp. 4462–4472). These results enrich our understanding of quasi-2-D thermal convection, and its similarities and differences compared to 2-D and 3-D systems.

Key words: Bénard convection, plumes/thermals, turbulent convection

† Email address for correspondence: huangsd@sustech.edu.cn

1. Introduction

Thermal convection occurs widely in nature and industrial processes. Rayleigh–Bénard (RB) convection, a fluid layer confined between two horizontally parallel conducting plates with heating from below and cooling from above, is a paradigmatic model for studying generic thermal convection phenomena. This system is characterized by three dimensionless parameters, namely the Rayleigh number $Ra = \alpha g \Delta T H^3/(\nu\kappa)$, the Prandtl number $Pr = \nu/\kappa$ and the aspect ratio Γ (the lateral dimension of the fluid layer over its height H). Here, ΔT is the temperature difference across the fluid layer, g is the gravitational acceleration, and α, ν and κ are the thermal expansion coefficient, the kinematic viscosity and the thermal diffusivity of the working fluid, respectively. The response of the system is generally quantified by the heat transfer efficiency and flow strength, which are indicated by the Nusselt number Nu and the Reynolds number Re, respectively.

Over the past decades, extensive studies have been devoted to understand how the heat transport and the flow dynamics of turbulent RB convection are determined by the three control parameters mentioned above (Ahlers, Grossmann & Lohse 2009; Lohse & Xia 2010; Chillà & Schumacher 2012). Recently, there have been increasing interests that go beyond the conventional RB configuration by modifying the boundary condition and geometric structure of the system. Examples include creating different roughness patterns over the conducting plates (Wagner & Shishkina 2015; Toppaladoddi, Succi & Wettlaufer 2017; Xie & Xia 2017; Rusaouën *et al.* 2018; Zhang *et al.* 2018; Foroozani *et al.* 2019; Zhu *et al.* 2019; Emran & Shishkina 2020), tilting the convection cell with a broad range of inclination angle (Guo *et al.* 2015; Shishkina & Horn 2016; Wang *et al.* 2018; Jiang, Sun & Calzavarini 2019; Zwirner *et al.* 2020), using mixed or time-modulated thermal boundary conditions (Ripesi *et al.* 2014; Wang, Huang & Xia 2017; Bakhuis *et al.* 2018; Yang *et al.* 2020*a*), adding partitioned structures inside the convection cell (Bao *et al.* 2015; Chen *et al.* 2017; Liu *et al.* 2020) and even applying vibration to the system (Wang, Zhou & Sun 2020*a*). Nevertheless, there still remain many issues to be explored for the classical RB system.

One relatively less addressed issue in the study of classical RB convection is the effect of the Pr number, especially compared to the large body of studies over a wide range of Ra number. The existing studies on this issue were mostly made in convection cells with three-dimensional (3-D) geometry (Globe & Dropkin 1959; Verzicco & Camussi 1999; Kerr & Herring 2000; Ahlers & Xu 2001; Lam *et al.* 2002; Roche *et al.* 2002; Xia, Lam & Zhou 2002; Breuer *et al.* 2004; Silano, Sreenivasan & Verzicco 2010; Stevens, Lohse & Verzicco 2011; Shishkina *et al.* 2017; Yang *et al.* 2020*b*). According to these studies, two different scaling regimes were identified based on the Pr dependences of the Nu and Re numbers: Nu first increases strongly with Pr for $Pr \lesssim 1$, and then, after reaching a maximum at $Pr \simeq 3$, it gradually decreases with Pr and can be described by a power law as $Nu \sim Pr^{-0.03}$ approximately; the Pr-dependent scaling of Re also possesses a transition around $Pr \simeq 1$. These findings were in good agreement with the predictions of the Grossmann–Lohse (GL) model (Grossmann & Lohse 2000, 2001, 2002; Stevens *et al.* 2013), which, in essence, are based on two-dimensional (2-D) equations.

However, the numerical simulations in the 2-D system show different behaviours compared to the 3-D case. Schmalzl, Breuer & Hansen (2004) first found that the Nu data in 2-D RB convection at $Ra = 10^6$ have no obvious Pr dependence in the range of $10^{-2} \leqslant Pr \leqslant 10^2$, and Re differs from the 3-D data when Pr is smaller than unity.

By extending the Ra number up to $Ra = 10^{10}$, later numerical studies showed that Nu is insensitive to Pr when Pr is greater than 10 (van der Poel *et al.* 2012; van der Poel, Stevens & Lohse 2013; He *et al.* 2021). It was further found that the strong counter-gradient local heat flux in the 2-D configuration can lead to an anomalous Nu–Pr relation, i.e. Nu minimizes at $Pr \approx 2$–3, rather than maximizes as found in the 3-D case (Huang & Zhou 2013). Moreover, the Re number in 2-D RB flow not only has a larger magnitude, but also exhibits a notably different Ra–Pr dependence from the 3-D case (van der Poel *et al.* 2013; Zhang, Zhou & Sun 2017).

The reasons for these discrepancies between 2-D and 3-D RB systems were assessed to be twofold (Schmalzl *et al.* 2004; van der Poel *et al.* 2013; Pandey *et al.* 2016). The first one comes from the large-scale circulation (LSC). Although the LSC in the 3-D system has a quasi-2-D geometrical character (Xi & Xia 2008; Sugiyama *et al.* 2010), its dynamical features are fully 3-D and cannot be resembled by the 2-D flow. The second one is related to thermal plumes. While the movement and evolution of thermal plumes in 2-D geometry are restrained in the third dimension, these limitations are not as great in 3-D. In fact, the two reasons are correlated with each other, and both could be attributed to the effects of spatial confinement. Recent studies showed that spatial confinement can result in pronounced changes in the morphology and dynamics of thermal plumes, which bring about very different large-scale flow dynamics and unexpected heat transport enhancement (Huang *et al.* 2013; Chong *et al.* 2015; Chong & Xia 2016; Huang & Xia 2016). As the LSC in the 3-D RB system is essentially a quasi-2-D structure, and the influences of spatial confinement depend strongly on Pr (Wagner & Shishkina 2013; Chong *et al.* 2018), it is natural to ask: How does the Pr number influence RB convection in quasi-2-D geometry? To the best of our knowledge, this issue has not been investigated experimentally before.

For quasi-2-D RB convection, it is generally considered that the LSC is limited to a quasi-2-D plane without complicated 3-D dynamics, such as azimuthal rotation and torsional motion (Sugiyama *et al.* 2010). In the present study, we used rectangular convection cells with the same geometrical features as in previous experiments (Huang *et al.* 2015; Chen *et al.* 2019), i.e. the aspect ratio in the plane parallel to the LSC is unity, whereas that perpendicular to the LSC is 0.3. Four such convection cells with different sizes were used to cover the Ra number range of $6.0 \times 10^8 \leqslant Ra \leqslant 3.0 \times 10^{10}$ and the Pr number range of $11.7 \leqslant Pr \leqslant 650.7$. It is found that the LSC breaks down for higher Pr, resulting in a regime transition in the Re number. For the Pr range with a persistent LSC, both the Re and Nu numbers were investigated systematically and compared to the behaviours in 2-D and 3-D systems. In addition to these commonly measured global properties, we also examined the effect of Pr on local temperature fluctuations, which has received little attention so far (Daya & Ecke 2002; Grossmann & Lohse 2004; Wunsch & Kerstein 2005; Chong *et al.* 2018). These experimental results not only enrich our knowledge of classical RB convection in quasi-2-D geometry, but also provide a useful basis for studying non-traditional thermal convection systems.

The remainder of this paper is organized as follows. The experimental set-up and methods are introduced in § 2. The main results are presented in § 3, which is divided into four parts. In § 3.1, we first show the flow patterns obtained with the shadowgraph technique for different Pr numbers. Then we present and discuss the behaviour of the Re number in § 3.2, followed by the Nu number in § 3.3. The local temperature fluctuations measured in the cell centre and near the sidewall will be presented in § 3.4. Finally, we summarize the findings in § 4.

2. Experimental apparatus and methods

As shown in table 1, there are eight datasets in total obtained in the present study. To vary the Pr number from 11.7 to 650.7, seven kinds of silicone oil (KF-96 series, Shin-Etsu Inc.) were used as the working fluids. Their fluid properties were provided by Shin-Etsu and verified by independent measurements from a commercial company (Netzsch Inc.). In contrast to previous experiments where the Ra range always changes for different Pr (Ahlers & Xu 2001; Lam *et al.* 2002; Roche *et al.* 2002; Xia *et al.* 2002; Yang *et al.* 2020*b*), we used four convection cells with the same aspect ratios but different sizes to maintain Ra with the same values while varying Pr (see table 1 for the geometrical information on the convection cells and the corresponding parameter ranges). Having almost identical Ra numbers is one important feature of the present study, as it allows us to compare the results from different Pr directly. In addition, we have made measurements at $Pr = 20.5$ in two different cells (datasets II and III), so that we can examine the effect of system size if there is any.

The four convection cells used in the experiments were of identical design (Zhou *et al.* 2012) and their schematic diagram is shown in figure 1(*a*). Briefly, they were built independently with their own conducting copper plates and Plexiglas sidewalls. The heat flux Q was supplied to the bottom plate by a nichrome wire and extracted at the top plate by a recirculating cooler. The temperatures of the bottom and top plates were monitored by thermistors (Omega, Model 44031) embedded uniformly inside the plates (not shown in the figure), based on which we obtained the temperature difference across the fluid layer ΔT, and then the Nu number can be calculated as $Nu = QH/(\chi \Delta T)$. Here, χ is the thermal conductivity of the working fluid. The temperatures inside the fluid were measured by three small thermistors with a tip size of $\sim$200 μm (Measurement Specialties, Model G22K7MCD419). As shown in figure 1(*a*), they were mounted on stainless-steel tubes of 1 mm diameter. Thermistor T_1 was used to monitor the temperature in the cell centre, which was maintained at 40.0 °C for all the measurements.

In addition to acquiring local temperatures, thermistors T_2 and T_3 were further used to detect the motion of thermal plumes near the sidewall of the convection cell. This method (Wang *et al.* 2016) is based on the idea that, when thermal plumes pass through a region, they will result in appreciable temperature variations in the background flow, and the two temperature sensors with a small separation d should experience similar variations with a time delay (see the inset of figure 1*b*). By calculating the correlation function between the signals of T_2 and T_3 (figure 1*b*), we can identify the mean time delay τ and then obtain the velocity $U = d/\tau$. Finally, the corresponding Re number based on plume motion can be expressed as $Re = 2HU/\nu = 2Hd/\tau\nu$, where $2H$ has been used for the typical length scale as in most previous studies (Ahlers *et al.* 2009). Because the flow velocity strongly depends on the distance away from the sidewall and the flow pattern continuously evolves while varying Ra and Pr (Niemela & Sreenivasan 2003; Xia, Sun & Zhou 2003; Belkadi *et al.* 2020), both of which will affect the measured value of the Re number, we adjusted the positions of T_2 and T_3 at different (Ra, Pr) settings to make sure that they were located in the region near the sidewall where most organized plumes passed through (see table 4 in the appendix for their distance away from the sidewall). Therefore, the so-obtained U and Re can well represent the characteristic velocity and strength of the flow, respectively.

Note that in cases where direct measurement of velocity field is difficult, various other methods have been developed to estimate the Re number. For example, Chavanne *et al.* (2001) used the cross-correlation spectrum method, He, He & Tong (2010) applied the elliptic approximation (He & Zhang 2006), and Belkadi *et al.* (2020) even derived an estimate from the shadowgraph images. These different methods would lead to very

Dataset	$H \times L \times W$	Pr	Ra	α ($\times 10^{-3}$)	κ ($\times 10^{-8}$)	ν ($\times 10^{-6}$)
I	$12.6 \times 12.6 \times 3.8$	11.7	6.7×10^8 to 2.1×10^{10}	1.29	6.43	0.755
II	$12.6 \times 12.6 \times 3.8$	20.5	6.7×10^8 to 6.0×10^9	1.24	7.36	1.51
III	$25.2 \times 25.2 \times 7.6$	20.5	2.4×10^9 to 3.0×10^{10}	1.24	7.36	1.51
IV	$25.2 \times 25.2 \times 7.6$	49.3	6.0×10^8 to 2.1×10^{10}	1.09	7.65	3.77
V	$37.8 \times 37.8 \times 11.3$	81.6	1.0×10^9 to 2.7×10^{10}	1.06	9.24	7.55
VI	$50.4 \times 50.4 \times 15.1$	145.7	1.0×10^9 to 2.1×10^{10}	1.04	1.04	1.51
VII	$50.4 \times 50.4 \times 15.1$	345.2	1.5×10^9 to 1.4×10^{10}	0.96	10.9	37.7
VIII	$50.4 \times 50.4 \times 15.1$	650.7	6.7×10^8 to 3.5×10^9	0.95	11.6	75.5

Table 1. Geometrical information on the convection cells for different Pr numbers and the corresponding Ra number ranges. Here, H (cm), L (cm) and W (cm) are the height, length and width of the convection cell, respectively. The fluid properties of the silicone oils used in the present study are also provided, where α (K^{-1}), κ ($m^2\ s^{-1}$) and ν ($m^2\ s^{-1}$) are the thermal expansion coefficient, the thermal diffusivity and the kinematic viscosity, respectively.

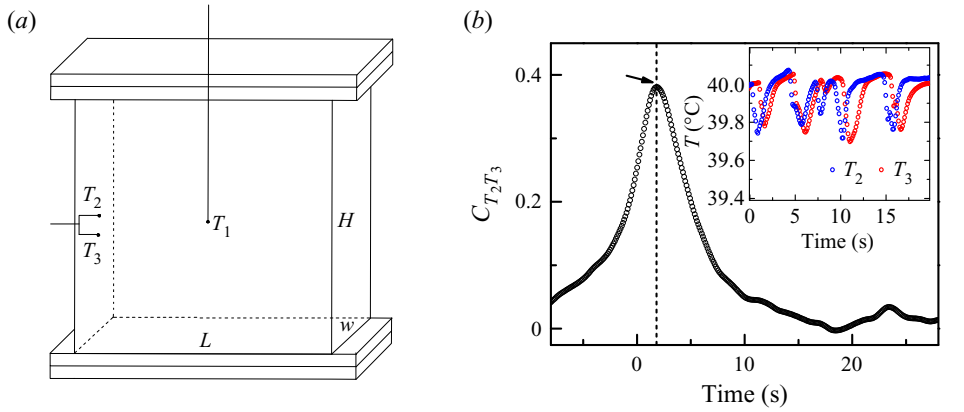

Figure 1. (*a*) Schematic diagram of the experimental set-up. Here T_1, T_2 and T_3 indicate three small thermistors used to measure local temperature in the flow. (*b*) The correlation function between the signals measured by T_2 and T_3, based on which we can obtain the characteristic flow velocity. See text for the explanation. Inset: A segment of the temperature time series measured by T_2 and T_3 at $Ra \simeq 5.9 \times 10^9$ and $Pr = 49.3$.

different values of Re and thus it does not help to make a comparison of their magnitudes directly. On the other hand, when considering the scaling exponents of $Re(Ra, Pr)$, the differences between the various methods are relatively small (see e.g. Ahlers *et al.* (2009) for a review and also the recent study by Musilová *et al.* (2017)). Therefore, in the present study, we will not compare the magnitude of our measured Re with other published data, but just focus on the scaling exponents of $Re(Ra, Pr)$.

Before the measurements at each dataset, we first used the shadowgraph technique (Xi, Lam & Xia 2004) to visualize the flow and obtain an overall picture of the Pr effects on the flow dynamics and plume distribution. This information also helped us to determine the positions of the two thermistors T_2 and T_3 mentioned above. Then we began the measurements of Re, Nu and local temperatures, which lasted at least 10 h for each (Ra, Pr) setting. To minimize the heat exchange from system to the surroundings, the convection cell was wrapped by thermal insulating Styrofoam with a thickness of ∼8 cm.

Furthermore, a size-matched copper basin was placed under the convection cell with three layers of plywood in between. A minor heat flux was provided to the copper basin to keep its temperature equal to that of the bottom plate, so that the heat loss from the bottom plate can be compensated. Finally, the whole apparatus was placed inside a thermostat to prevent any influence from the environment. Such a configuration has been demonstrated to ensure heat transport measurement with high precision (Ni, Zhou & Xia 2011*b*; Wei, Ni & Xia 2012) and we have adapted it in recent studies of quasi-2-D RB convection (Huang *et al.* 2013; Huang & Xia 2016).

In order to satisfy the Oberbeck–Boussinesq (OB) approximation, we paid close attention to the non-OB effect, which is characterized by the ratio of the temperature drops across the bottom and top boundary layers, $x = (T_b - T_c)/(T_c - T_t)$ (Wu & Libchaber 1991; Zhang, Childress & Libchaber 1997), where T_b, T_t and T_c are the measured temperatures of the bottom plate, the top plate and the cell centre, respectively. It was found that the values of x were in the range of $0.95 \leqslant x \leqslant 1.02$ without obvious Pr dependence. Thus the non-OB effect can be safely neglected in the present study (Ahlers *et al.* 2006).

3. Results and discussion

3.1. *Flow pattern*

We first examine how the flow pattern in quasi-2-D geometry responds to the Pr number. Figure 2 shows the shadowgraph images of typical flow pattern for different Pr at $Ra \simeq 3.6 \times 10^9$. (See also Movie 1 in the supplementary movies available at https://doi.org/10.1017/jfm.2021.21.) The flow pattern at $Pr = 49.3$ is similar to that at $Pr = 20.5$, so its image is not shown here for the sake of the figure's layout. It is seen that, as Pr increases from 11.7 to 145.7, thermal plumes pass through the bulk region much less frequently, and their self-organized large-scale motion is more confined along the periphery of the convection cell. However, as Pr further increases to 345.2 and 650.7, the flow patterns totally change. Rather than moving along the sidewalls to form a system-sized LSC, thermal plumes at these two Pr preferentially rise up (fall down) in random locations of the convection cell and pass through the bulk region in a more straight way. Some plumes are so long-lived that they extend the entire height of the convection cell.

These changes are more evident for larger Ra as shown in figure 3. Compared to lower Ra, a major difference for the larger Ra cases is that the number of plumes increases significantly and they are more fragmentary thanks to stronger turbulent mixing. What is interesting here is that, for $Pr = 345.2$ at $Ra = 1.4 \times 10^{10}$ (the highest Ra that can be achieved for this Pr in the present study), the flow state seems to switch between random motion of thermal plumes and two organized rolls (see Movie 2 in the supplementary movies available at https://doi.org/10.1017/jfm.2021.21). This phenomenon implies that, before building up a system-sized LSC, there could be a metastable state in the form of a two-roll structure during the evolution of the flow pattern. We also increased the Ra number for $Pr = 650.7$ to as high as 5.0×10^9, but the LSC is still absent. Note that the thermal insulating Styrofoam was removed during the flow visualization, so detailed flow patterns might be affected due to heat leakage through sidewalls. Nevertheless, the disappearance of the LSC and the change in plume distribution are well reflected by the behaviours of Re and local temperature fluctuations, which will be presented in detail below.

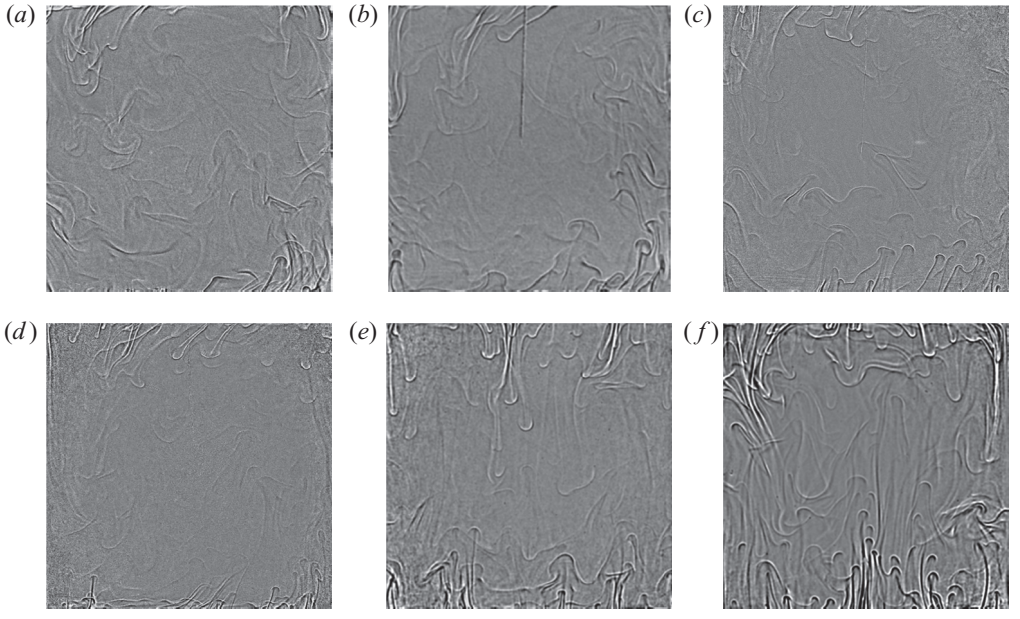

Figure 2. Shadowgraph images of the flow pattern at $Ra \simeq 3.6 \times 10^9$ for different Pr: (*a*) $Pr = 11.7$, (*b*) $Pr = 20.5$, (*c*) $Pr = 81.6$, (*d*) $Pr = 145.7$, (*e*) $Pr = 345.2$ and (*f*) $Pr = 650.7$. See also Movie 1 in the supplementary movies available at https://doi.org/10.1017/jfm.2021.21.

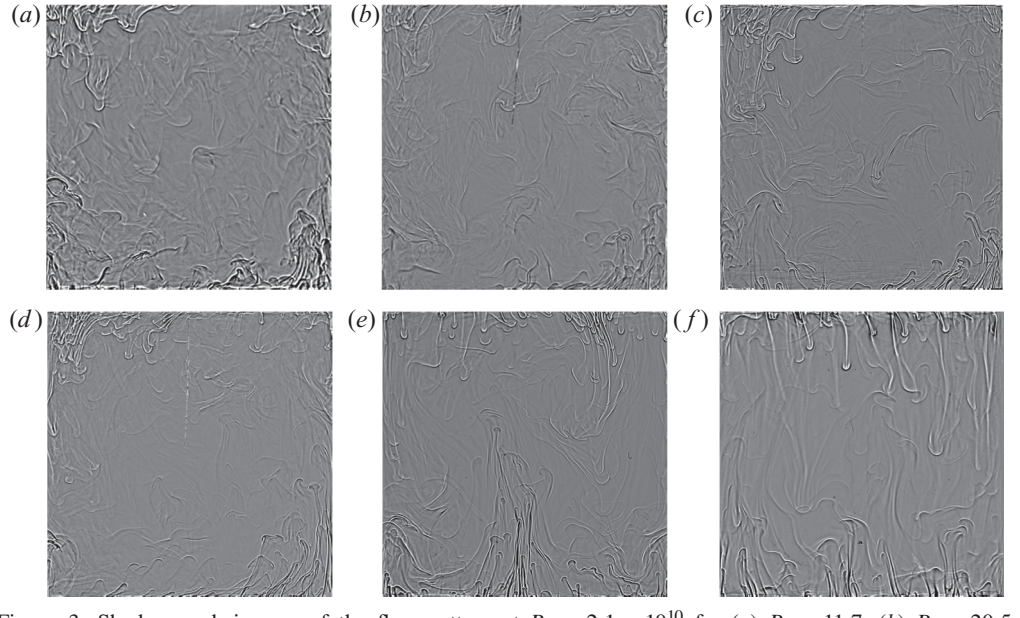

Figure 3. Shadowgraph images of the flow pattern at $Ra \simeq 2.1 \times 10^{10}$ for (*a*) $Pr = 11.7$, (*b*) $Pr = 20.5$, (*c*) $Pr = 81.6$ and (*d*) $Pr = 145.7$. Shadowgraph images of the flow pattern for (*e*) $Ra = 1.4 \times 10^{10}$, $Pr = 345.2$ and (*f*) $Ra = 5.0 \times 10^9$, $Pr = 650.7$. See also Movie 2 in the supplementary movies available at https://doi.org/10.1017/jfm.2021.21.

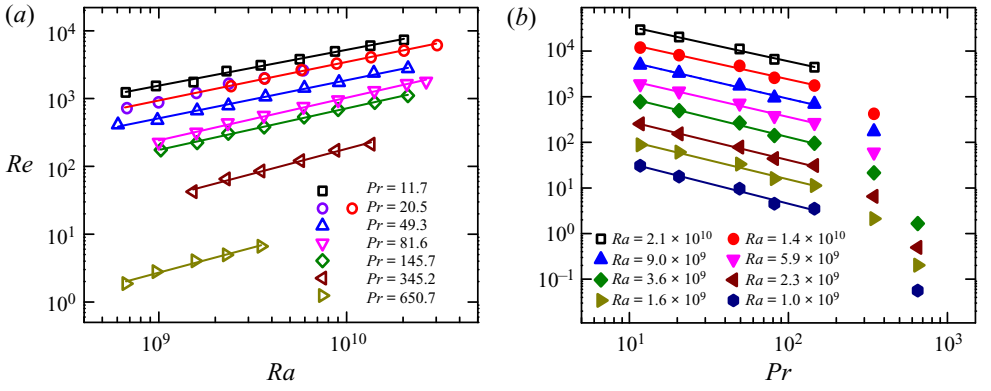

Figure 4. Log–log plots of (*a*) *Re* versus *Ra* for different *Pr* and (*b*) *Re* versus *Pr* for different *Ra*, as indicated by the symbols. For clarity, the data in panel (*b*) have been shifted by multiplication by different constant factors for different *Ra*. The solid lines represent power-law fits to individual datasets. See tables 2 and 3 in the appendix for the fitting results in detail.

3.2. *Reynolds number*

From the shadowgraph supplementary movies, it is also found that the flow motion becomes slower with increasing *Pr*. To quantify this effect, we examine the *Re* number obtained by the method as introduced in § 2. Figure 4(*a*) shows *Re* as a function of *Ra* for different *Pr*. Note that the data for $Pr = 20.5$ were measured at two convection cells with different sizes. Their almost identical values in the overlapping *Ra* range confirm that *Re* has no dependence on system size (Huang *et al.* 2015), so we will not distinguish them hereafter. From figure 4(*a*), it is seen that *Re* keeps decreasing as *Pr* increases, and the decrease becomes much larger when *Pr* goes to 345.2 and 650.7. The dramatic drop in *Re* at larger *Pr* well reflects the breakdown of the LSC. Besides the magnitude, the *Ra*-dependent scaling also exhibits a sudden change. For $11.7 \leqslant Pr \leqslant 145.7$, the scaling exponents (see table 2 in the appendix for detailed values) are close to each other, despite there being a slight change from 0.53 to 0.60. These values are consistent with the experimental finding (∼0.55) in similar convection cells for $Pr \simeq 4$–7 (Chen *et al.* 2019). However, the dependence becomes noticeably stronger for higher *Pr*, with the exponents being 0.73 and 0.74 for $Pr = 345.2$ and 650.7, respectively. A similar sudden growth of *Re*–*Ra* scaling (from 0.5 to 0.68) at high *Pr* has been observed previously in cylindrical convection cells, but there was no explanation for that in those studies (Lam *et al.* 2002; Silano *et al.* 2010). Here, with the information from direct flow visualization, we understand that this is a regime transition that originates from the change in large-scale flow.

The existence of two distinct regimes for *Re* is more obvious in figure 4(*b*). While the *Re* numbers at different *Ra* obey similar power laws in the range of $11.7 \leqslant Pr \leqslant 145.7$ (see table 3 in the appendix for detailed fitting results), the data at higher *Pr* follow a totally different trend. It could be that the convective flow has entered into the severely confined regime (Chong & Xia 2016), where the flow topology is also characterized by long-lived thermal plumes, and the *Re*–*Ra* scalings found there (0.69–0.80 for $Pr = 4.38$) are compatible with the present steep values. However, the limited data in the high-*Pr* regime prevent us from further examining their behaviours quantitatively in the present study. On the other hand, overwhelming studies of turbulent RB convection were conducted in the case with a well-defined LSC (Ahlers *et al.* 2009). The presence of an LSC is

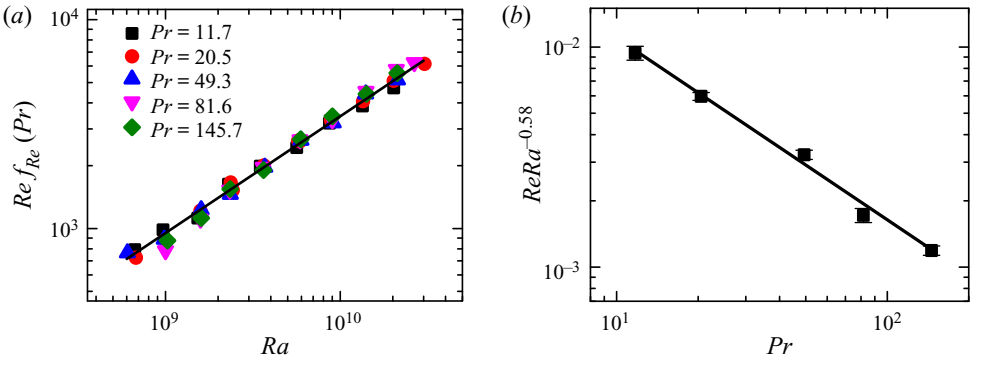

Figure 5. (*a*) Plot of $Re f_{Re}(Pr)$ as a function of Ra. Here, $f_{Re}(Pr)$ is a factor used to multiply the measured Re data such that the obtained results $Re f_{Re}(Pr)$ at different Pr collapse onto a single line. Note that the factor $f_{Re}(Pr)$ depends on Pr only and thus it is a constant for the dataset at each Pr. The solid line is the best power-law fit to all the data points: $Re f_{Re}(Pr) = 0.006 Ra^{0.58\pm0.01}$. (*b*) Plot of $ReRa^{-0.58}$ as a function of Pr. The data are mean values of $ReRa^{-0.58}$ averaged over all the Ra numbers for each Pr. The solid line represents a power-law fit: $ReRa^{-0.58} = 0.074 Pr^{-0.82\pm0.04}$.

also one central assumption of the widely accepted GL model (Grossmann & Lohse 2000). Therefore, in order to make a meaningful comparison with previous studies and model predictions, we henceforth focus on the flow properties (i.e. Re, Nu and temperature fluctuations) when an LSC is persistent. The Pr effects on RB convection without an LSC will be subject to more systematic studies in the future.

Before comparing our data with previous results obtained in other geometries, we follow the procedure used by Xia *et al.* (2002) to obtain a simple $Re(Ra, Pr)$ relation in the range of $11.7 \leqslant Pr \leqslant 145.7$. To be specific, the measured Re data are first multiplied by a factor $f_{Re}(Pr)$ such that the obtained results $Re f_{Re}(Pr)$ at different Pr collapse onto a single line properly (see figure 5*a*). Note that the factor $f_{Re}(Pr)$ depends on Pr only and thus it is a constant for the dataset at each Pr. After determining the best collapse of $Re f_{Re}(Pr)$ by a standard least-squares method, we made a power-law fit to all the data points in figure 5(*a*) and obtained the relation $Re f_{Re}(Pr) \sim Ra^{0.58\pm0.01}$. Then we normalize Re with $Ra^{0.58}$ and average the data over all the Ra at each Pr, with the results shown in figure 5(*b*). Finally, we obtain a unified description of Re in the present geometry and parameter ranges as $Re \sim Ra^{0.58\pm0.01} Pr^{-0.82\pm0.04}$.

The Ra-dependent scaling is in good agreement with the value of $\sim$0.6 for 2-D RB convection with non-slip walls (Sugiyama *et al.* 2009; van der Poel *et al.* 2013; Zhang *et al.* 2017; He *et al.* 2021), but is noticeably larger than those (varying from 0.4 to 0.5) found in the 3-D case (Ahlers *et al.* 2009). It is noteworthy that some recent numerical studies of 2-D RB convection with free-slip walls also observed a steep Re–Ra scaling close to 0.6 (Wang *et al.* 2020*b*; Wen *et al.* 2020).

For the Pr dependence, the scaling exponent in 2-D simulation varies from -0.91 to -0.81 for $10^8 \leqslant Ra \leqslant 10^{10}$ (van der Poel *et al.* 2013; He *et al.* 2021), which is compatible with the finding here (see also table 3 in the appendix). On the other hand, the Pr scaling observed in the 3-D system diverges a lot, depending mainly on the characteristic velocity used and the parameter ranges explored (Lam *et al.* 2002; Breuer *et al.* 2004; Brown, Funfschilling & Ahlers 2007; Silano *et al.* 2010; Yang *et al.* 2020*b*). If we consider Re based on the directed measured LSC velocity (close to the definition of the present study), the Pr scaling changes from -0.88 to -0.95 in a similar Ra–Pr range (Lam *et al.* 2002).

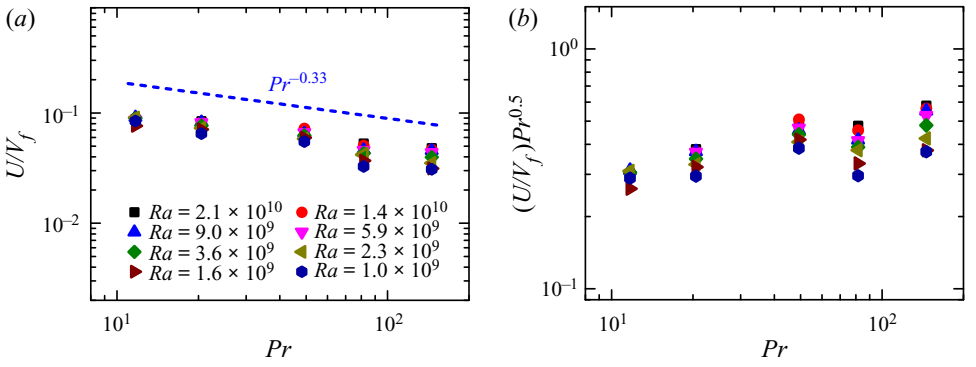

Figure 6. Plots of (*a*) U/V_f and (*b*) $(U/V_f)Pr^{0.5}$ as functions of Pr. Here, U is the characteristic velocity as explained in § 2 and V_f is the free-fall velocity. The dashed line in panel (*a*) shows the best-fitting exponent if a power-law fit is attempted to all the data points therein.

Combining the comparisons above, we conclude that the Re number in quasi-2-D RB convection is in line with that in the 2-D system.

To gain a better understanding of the present $Re(Ra, Pr)$ relation, it is worth pointing out that, if the characteristic flow velocity is a free-fall type, i.e. $V_f = \sqrt{\alpha g \Delta T H}$, the corresponding Re number scales with Ra as $Re_{V_f} \sim Ra^{0.5}$. For RB convection in three dimensions, while the scaling of $Re(Ra)$ is often found to be similar to the free-fall type, the flow is slowed down considerably by viscous drag and the scaling is in general smaller than 0.5 (Ahlers *et al.* 2009). Thus, the Ra scaling value of $\sim$0.6 observed in (quasi-)2-D RB convection suggests that there could be another mechanism affecting the flow dynamics in these geometries. Interestingly, the Re–Ra scaling predicted by the GL model at very large Pr (say, $Pr \gtrsim O(10^3)$) is around 0.6 (Grossmann & Lohse 2000, 2001, 2002). One important feature of RB convection at very large Pr is the vanishing of the toroidal component in the flow, which is also the major difference between the (quasi-)2-D and 3-D systems (Schmalzl *et al.* 2004; van der Poel *et al.* 2013; Pandey *et al.* 2016). Therefore, from the viewpoint of large-scale dynamics, the present relation $Re \sim Ra^{0.58}$ could be related to the absence of toroidal motion in the third dimension.

On the other hand, varying Pr number not only has an effect on the advective dynamics, but also changes the diffusive property directly. Both processes play a role in the Re–Pr dependence. To distinguish between these two effects, we normalize the measured velocity U with the free-fall velocity V_f. In this way, the behaviour of U/V_f mainly reflects the role of the kinematic viscosity. As shown in figure 6(*a*), U/V_f is a decreasing function of Pr that follows an effective power law $Pr^{-0.33}$ approximately. Considering that the Re number based on V_f scales with Pr as $Re_{V_f} \sim Pr^{-0.5}$, this effective power law $Pr^{-0.33}$ represents how the diffusive dynamics contributes the Re–Pr dependence in the present Pr range, and it is consistent with the measured relation $Re \sim Pr^{-0.82}$. In a previous study, it was suggested that the free-fall velocity should be multiplied by $1/\sqrt{Pr}$ in order to account for the diffusive dynamics in RB convection at high Pr (Silano *et al.* 2010). To check this, we normalize the measured velocity U accordingly and plot the data in figure 6(*b*). Indeed, $(U/V_f)Pr^{0.5}$ first increases with Pr and then seems to be saturated when $Pr \gtrsim 50$, which is in agreement with the numerical results in Silano *et al.* (2010). This saturation provides experimental support that $V_f/\sqrt{Pr}$ is a more appropriate quantity to represent the characteristic large-scale velocity at high Pr.

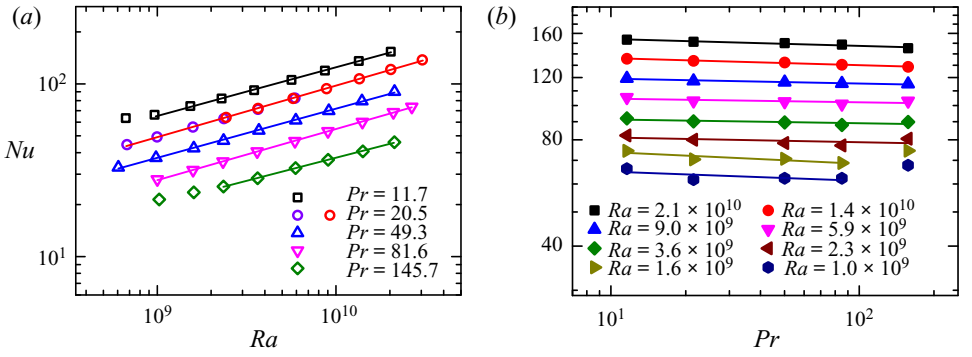

Figure 7. Plots of Nu as a function of (*a*) Ra for different Pr and (*b*) Pr for different Ra, as indicated by the symbols. For clarity, the data in panel (*a*) have been shifted by multiplication by the different constant factors shown for different Pr. The solid lines represent power-law fits to individual datasets with the fitting results shown in tables 2 and 3.

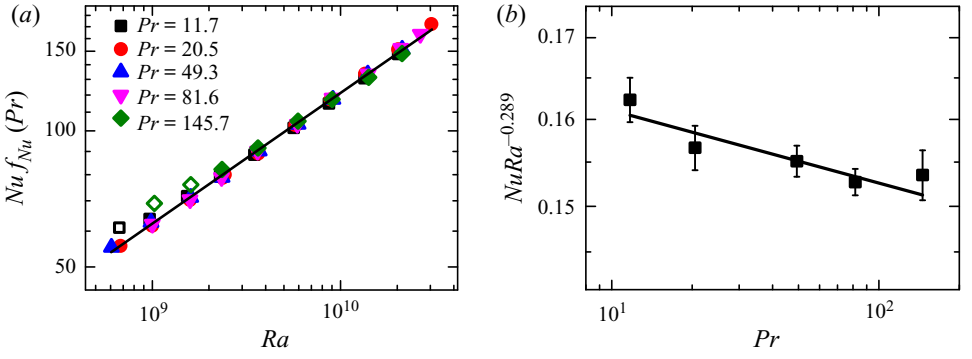

Figure 8. (*a*) Plot of $Nuf_{Nu}(Pr)$ as a function of Ra. Here, $f_{Nu}(Pr)$ is a factor used to multiply the measured Nu data such that the obtained results $Nuf_{Nu}(Pr)$ at different Pr collapse onto a single line. Note that the factor $f_{Nu}(Pr)$ depends on Pr only and thus it is a constant for the dataset at each Pr. The solid line is the best power-law fit to all the data points except for the open symbols: $Nuf_{Nu}(Pr) = 0.16Ra^{0.289\pm0.002}$. (*b*) Plot of Nu compensated by $Ra^{0.289}$ as a function of Pr. The data are the mean values of $NuRa^{-0.289}$ averaged over different Ra at each Pr. The solid line is a power-law fit: $NuRa^{-0.289} = 0.17Pr^{-0.02\pm0.01}$.

3.3. *Heat transport*

In this section, we investigate how Pr number affects the heat transfer efficiency in quasi-2-D RB convection. As shown in figure 7(*a*), the Nu for $Pr = 20.5$ measured in two different cells fall on top of each other, indicating that the system size has no effect on global heat transport. For the data points at each Pr, they can be fitted by similar Ra-dependent power laws, with the scaling exponents varying from 0.27 to 0.30. These exponents are consistent with the results found in quasi-2-D geometry at $Pr \simeq 4$–7 (Zhou *et al.* 2012; Huang & Xia 2016). When considering the Pr dependence (figure 7*b*), Nu decreases slightly as Pr increases, and the Pr scaling varies only marginally from -0.01 to -0.03 in the Ra range explored. Note that there are three data points showing obvious deviations from the main power-law trend (see also the open symbols in figure 8*a*), which could be attributed to the heat leakage through the bottom plate at small ΔT (Wei *et al.* 2012; Zhou *et al.* 2012), so they are not included in the analysis here.

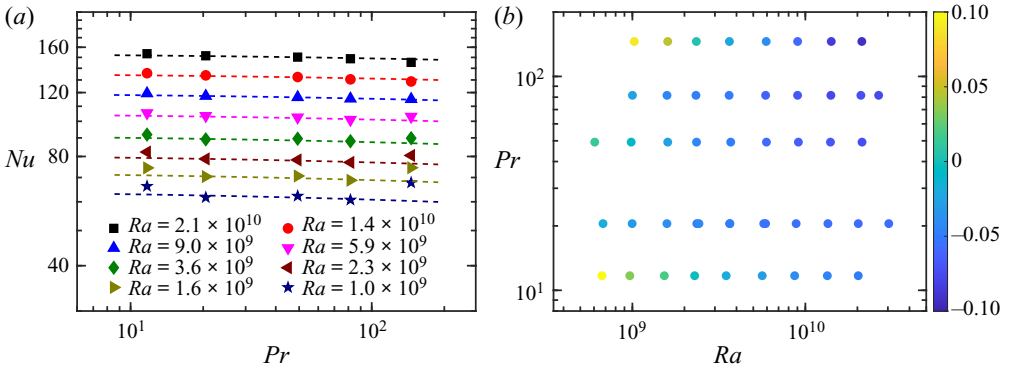

Figure 9. (*a*) The measured *Nu* compared with the values predicted by the updated GL model (Stevens *et al.* 2013). The dashed lines indicate the updated GL model predictions multiplied by 0.93, 0.93, 0.94, 0.94, 0.95, 0.96, 0.96 and 0.98 from highest to lowest *Ra*, respectively. (*b*) The relative difference in *Nu* between the present study and the GL model prediction, i.e. $(Nu - Nu_{GL})/Nu_{GL}$.

The similar scaling exponents allow us to extract a simple $Nu(Ra, Pr)$ relation as we did for the *Re* number. Briefly, the measured *Nu* data are multiplied by a factor $f_{Nu}(Pr)$ at each *Pr*, so that the obtained results $Nu f_{Nu}(Pr)$ at different *Pr* collapse onto a single line and can be well described by $Nu f_{Nu}(Pr) \sim Ra^{0.289}$ (figure 8*a*). Then we normalize *Nu* with $Ra^{0.289}$ and average the data over different *Ra* for each *Pr*. Finally, by making a power-law fit to the so-obtained results (figure 8*b*), we obtain that $Nu \sim Ra^{0.289} Pr^{-0.02}$. This scaling relation is in agreement with the previous finding in the 3-D system (Xia *et al.* 2002). The GL model also predicts that *Nu* is a decreasing function of *Pr* in the present parameter ranges (Grossmann & Lohse 2000; Stevens *et al.* 2013). However, the 2-D numerical data show that *Nu* is independent of *Pr* for $Pr \gtrsim 10$ (Schmalzl *et al.* 2004; van der Poel *et al.* 2013; He *et al.* 2021). In this context, we would conclude that the scaling relation of heat transport in quasi-2-D RB convection is compatible with the behaviour in 3-D.

In addition to scaling exponent, it is also interesting to check how the magnitude of *Nu* in the quasi-2-D RB system compares to the prediction of the GL model. In the past two decades, the GL model has achieved great success in describing heat transport behaviour in 3-D RB convection (Grossmann & Lohse 2000; Ahlers *et al.* 2009; Stevens *et al.* 2013). Recently, it has been further shown that the GL prediction is able to capture the *Nu* data in 2-D simulations, only differing by a constant factor (van der Poel *et al.* 2013; He *et al.* 2021). From figure 9(*a*), it is seen that, once the GL predicting curves are shifted down by certain constant factors, most of the data obtained in the present quasi-2-D system can be described by the GL model as well, but the shift factors (ranging from 0.93 to 0.98) are larger than those values (∼0.8) in the 2-D case.

To compare our experimental data with the GL model prediction directly, we show their relative difference in figure 9(*b*). It is seen that the measured *Nu* are systematically smaller than the GL predicted values, except for several data points. However, as these deviations are relatively small, it is unclear whether these differences could suggest that heat transfer in quasi-2-D RB convection is weaker than that in the 3-D situation. More studies and direct evidence are needed. Finally, it is noteworthy that, even after proper shifting, the GL prediction does not capture well most of the data at $Pr = 145.7$. A similar situation was found in the 3-D system (Xia *et al.* 2002), which was attributed to the uncertainty

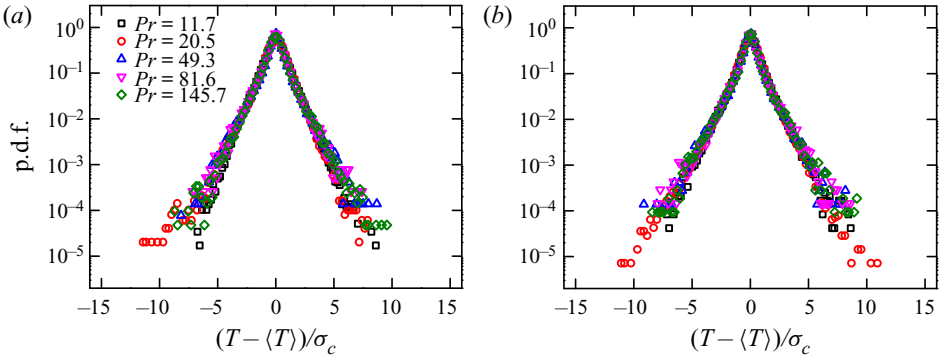

Figure 10. The p.d.f.s of temperature fluctuation measured in the central region of the convection cell for different Pr: (*a*) $Ra \simeq 3.6 \times 10^9$ and (*b*) $Ra \simeq 2.1 \times 10^{10}$.

in the experimental data at high Pr that are used to determine the GL model parameters (Stevens *et al.* 2013). In view of this discrepancy, more experimental measurements at high Pr are worthwhile.

3.4. *Local temperature fluctuations*

As revealed by the shadowgraph images, Pr number has a strong impact on the spatial distribution of thermal plumes. This change would consequently affect local temperature fluctuations in the flow. To investigate this effect quantitatively, we measured the temperature fluctuations in two representative regions of the convection cell, i.e. the central region where the turbulent background is dominant and the region near the sidewall with abundant amount of thermal plumes. Since the flow dynamics in these two regions are different, the corresponding flow properties should scale with different functions of Ra and Pr.

Figure 10 shows the probability density functions (p.d.f.s) of temperature fluctuation measured in the central region at two Ra numbers. It is seen that all the p.d.f.s exhibit a stretched exponential shape and have no systematic variation with respect to different parameters. However, their root-mean-square (r.m.s.) values are sensitive to the changes in Ra and Pr. One can see in figure 11(*a*) that the normalized temperature fluctuations $\sigma_c/\Delta T$ for all Pr decrease with a similar trend as Ra increases, but there is no clear Pr dependence. By taking a closer look at the seemingly messed data, it is found that the two datasets at $Pr = 20.5$ differ from each other unexpectedly. The results measured in the large cell with $H = 25.2$ cm (red open circles) are consistently larger than those in the small cell with $H = 12.6$ cm (purple open circles), despite the two convection cells having identical geometrical features (i.e. aspect ratios). Thus, in contrast to global properties, our data indicate that local temperature fluctuation can be affected significantly by the system size.

Similar size-dependent behaviours have been observed in previous experimental studies of other local properties in turbulent RB convection (Ni, Huang & Xia 2011*a*; Huang *et al.* 2015), but the physical origin remains elusive. In order to examine the effect of Pr number on local temperature fluctuations, we first use an empirical method to find out the size-dependent relation in the present study. To be specific, we shift down the data measured in the large cell by a constant factor, so that the shifted data (solid red circles in figure 11*b*) can collapse with the results in the small cell in the overlapped Ra

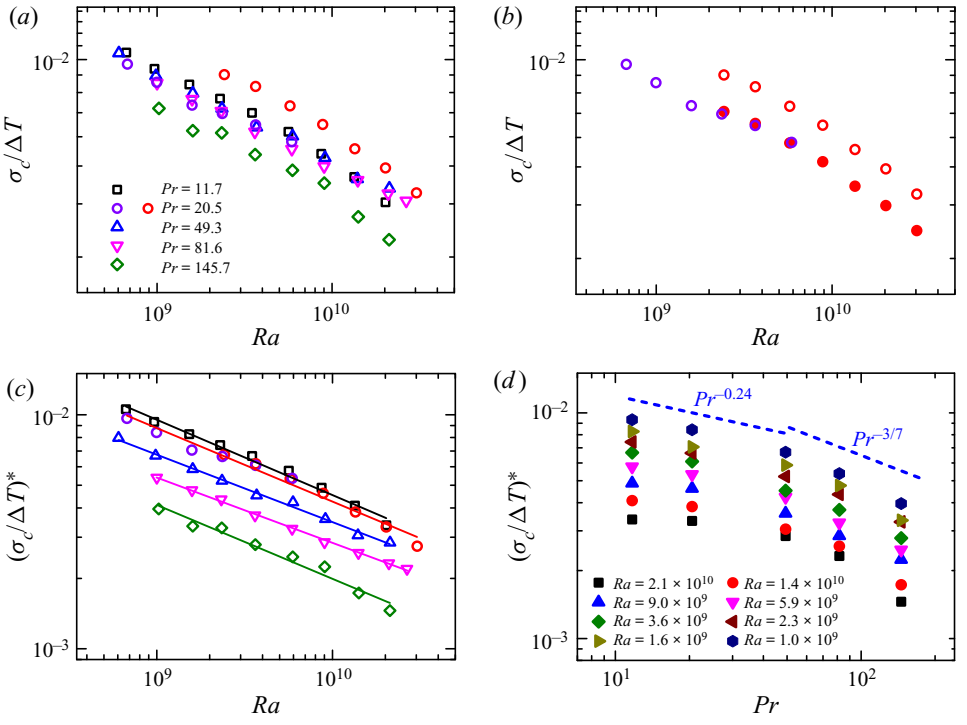

Figure 11. (*a*) Normalized temperature fluctuation $\sigma_c/\Delta T$ at the cell centre as a function of Ra for different Pr. (*b*) Plot of $\sigma_c/\Delta T$ for $Pr = 20.5$ measured at two convection cells. See text for detailed explanation. (*c*) Plot of $(\sigma_c/\Delta T)^*$ versus Ra as indicated by the same symbols as used in panel (*a*). Here, $(\sigma_c/\Delta T)^* = (\sigma_c/\Delta T)/(H/12.6)^{0.4}$ represents temperature fluctuation with the system size effect compensated. The solid lines are power-law fits to individual datasets with the fitting results listed in table 2. (*d*) Plot of $(\sigma_c/\Delta T)^*$ versus Pr for different Ra. The two dashed lines represent the predictions for interior temperature fluctuation by two different models. See text for explanation.

range. Inspired by the study of Ni *et al.* (2011*a*), the shift factor used has an H-dependent power-law form, which is determined by the best collapse of the data and turns out to be $(25.2/12.6)^{0.4}$. Following this relation, we rescale all the data by $(H/12.6)^{0.4}$, i.e. $(\sigma_c/\Delta T)^* = (\sigma_c/\Delta T)/(H/12.6)^{0.4}$, and plot them in figure 11(*c*). Note that this rescaling does not change the Ra dependence, but it might have an effect on the outcome of the Pr-dependent behaviour. After the rescaling, it is seen that the temperature fluctuation in the central region decreases with increasing Pr. This is consistent with the picture that both the number of thermal plumes and the flow strength are reduced in this region as Pr increases. This consistency qualitatively supports the validity of the size-dependent relation acquired here.

For $(\sigma_c/\Delta T)^*$ at each Pr, they can be well fitted by similar power laws with the scaling exponents being around -0.30 (see table 2 in the appendix for detailed values). These exponents are close to the finding (-0.35) obtained in a similar convection cell for $Pr = 4.3$ (Huang & Xia 2016), but are very different from those values (-0.10 to -0.17) found in the 3-D system (see e.g. Castaing *et al.* 1989; Daya & Ecke 2002; Wei *et al.* 2012; Xie *et al.* 2019) and the predictions (-0.11 to -0.16) of various existing models (Kraichnan 1962; Castaing *et al.* 1989; Grossmann & Lohse 2004; Wunsch & Kerstein 2005). Moreover, the approximate universal Ra dependence in the present geometry is in contrast to previous

measurements in a cylindrical convection cell (Daya & Ecke 2002). It was shown there that the *Ra* scaling exponent of the interior temperature fluctuation is a strong function of *Pr*. These discrepancies could be manifestations of different large-scale dynamics in different geometries (Daya & Ecke 2001), which have not been taken into account with existing models.

On the other hand, $(\sigma_c/\Delta T)^*$ shown in figure 11(*d*) precludes a simple scaling with respect to *Pr*; instead, they appears to be a cross-over of two different regimes that could be described by two different models. Notwithstanding the data scatter, $(\sigma_c/\Delta T)^*$ for $Pr \lesssim 50$ at most *Ra* cases follow the trend of a $Pr^{-0.24}$ power law, which is the prediction for turbulence-dominant temperature fluctuation by Grossmann & Lohse (2004). As *Pr* becomes larger, the data seem to agree with the prediction of the mixing zone and sheared boundary layer theories (Castaing *et al.* 1989; Shraiman & Siggia 1990; Daya & Ecke 2002). Although we have no explanation for why $(\sigma_c/\Delta T)^*$ at larger *Pr* is in line with the mixing zone and sheared boundary layer theories, the cross-over may be understood with the evolution of the turbulent features in the central region. While the flow in this region at small *Pr* is strongly violent and dominated by turbulent fluctuation as assumed by Grossmann & Lohse (2004), the bulk fluid becomes relatively quiet as *Pr* increases, and thus the assumption of the GL model is not satisfied in the high-*Pr* regime. The agreement between experimental data and model predictions confirms that the empirical relation acquired above is adequate for the first-order approximation.

When it comes to the region near the sidewall where a large amount of thermal plume pass through constantly, the behaviour of the temperature fluctuation becomes a bit more complex. It is seen in figure 12 that their p.d.f.s are not symmetric any more. This asymmetric shape can be understood with the flow pattern as seen in the shadowgraph supplementary movies. Firstly, the left skewed tail is mainly contributed by the cold downwelling plumes dominant in this region, which is similar to the 3-D system (Wei *et al.* 2012). For the minor peak in the right tail, it could be explained by the observation that some hot plumes detached from the corner are so strong that they reach the measured region from time to time. Besides the difference in shape, the p.d.f.s for different *Pr* could not collapse as well as that in the central region. To quantify these changes, we plot the normalized temperature fluctuation near the sidewall region $\sigma_s/\Delta T$ in figure 13(*a*). It is found that the temperature fluctuation in this plume-abundant region also depends on the system size, but the data obtained in the large cell have lower values than in the small cell, which is contrary to the dependence in the central region. Following the same procedure as used for $\sigma_c/\Delta T$, we find that the size-dependent relation for $\sigma_s/\Delta T$ is $(H/12.6)^{-0.55}$. The different size-dependent relations for different regions imply that, indeed, a local flow property should be used for the normalization.

Figures 13(*c*) and 13(*d*) show the temperature fluctuation with the system size effect compensated, i.e. $(\sigma_s/\Delta T)^* = (\sigma_s/\Delta T)/(H/12.6)^{-0.55}$, as functions of *Ra* and *Pr*, respectively. It is obvious that a single scaling is insufficient to describe all the data appropriately. Nevertheless, the data below $Ra \simeq 10^{10}$ could be well fitted by similar power laws, with the *Ra*-dependent exponents ranging around -0.18 (see table 2 in the appendix for fitting results). There are very few studies of temperature fluctuation near the sidewall in the literature. The limited results were all obtained in cylindrical convection cells and the *Ra*-dependent scalings differ a lot from each other, ranging from -0.15 to -0.24 (Shang, Tong & Xia 2008; Lakkaraju *et al.* 2012; Wei *et al.* 2012). Given the large discrepancy, we cannot conclude that the present *Ra*-dependent scaling in quasi-2-D geometry is consistent with the 3-D results, but we cannot discount it either. For the *Pr* dependence, it is seen in figure 13(*d*) that $(\sigma_s/\Delta T)^*$ can also be divided into two regimes at $Pr \simeq 50$: while the

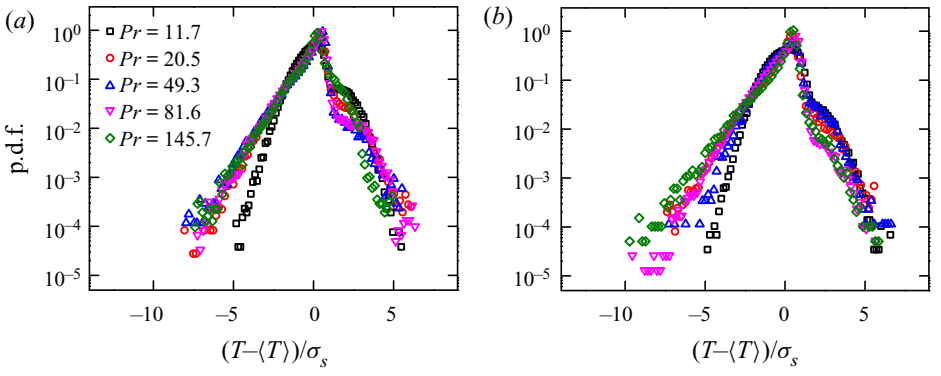

Figure 12. The p.d.f.s of temperature fluctuation measured near the sidewall of the convection cell for different Pr: (*a*) $Ra \simeq 3.6 \times 10^9$ and (*b*) $Ra \simeq 2.1 \times 10^{10}$.

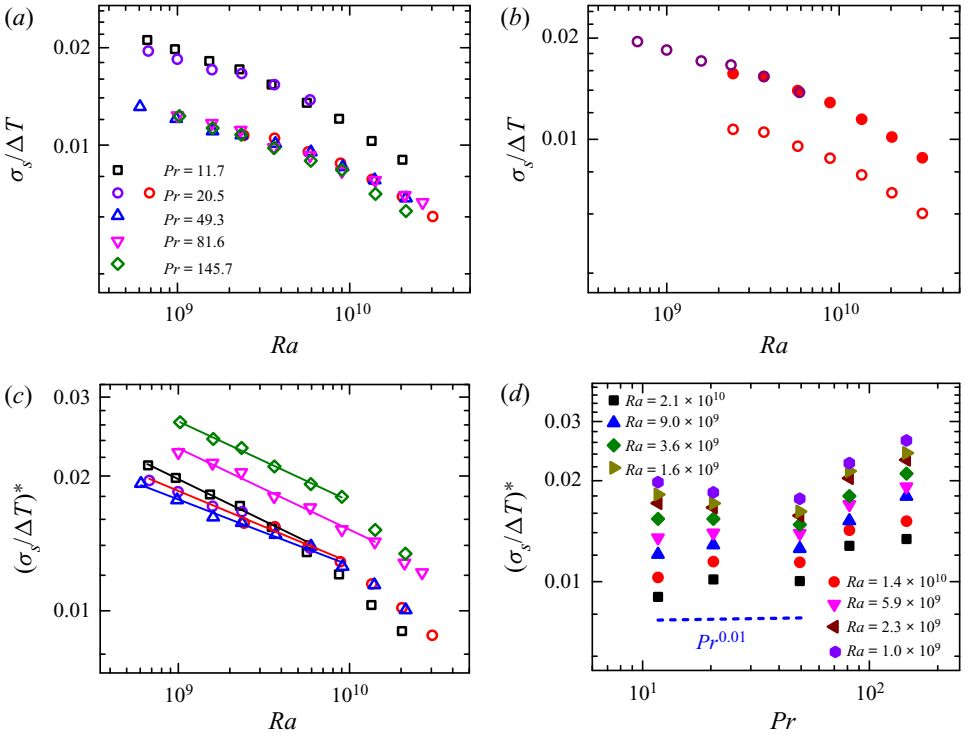

Figure 13. (*a*) Normalized temperature fluctuation $\sigma_s/\Delta T$ near the sidewall region as a function of Ra for different Pr. (*b*) Plot of $\sigma_s/\Delta T$ versus Ra for $Pr = 20.5$ measured at two convection cells. The symbols share the same meanings as in figure 11(*b*). (*c*) Plot of $(\sigma_s/\Delta T)^*$ versus Ra for different Pr as indicated by the same symbols as used in panel (*a*). Here, $(\sigma_s/\Delta T)^* = (\sigma_s/\Delta T)/(H/12.6)^{-0.55}$ represents temperature fluctuation with the system size effect compensated. The solid lines are power-law fits with the fitting results shown in table 2. (*d*) Plot of $(\sigma_s/\Delta T)^*$ versus Pr for different Ra. The dashed line represents the prediction by Grossmann & Lohse (2004) for temperature fluctuation close to the sidewall.

data for $Pr \lesssim 50$ is a weakly dependent function of Pr, they increase significantly when Pr becomes larger. By considering the role of thermal plumes explicitly, Grossmann & Lohse (2004) predict that the temperature fluctuation close to the sidewall scales with

Pr as $Pr^{0.01}$, which is compatible with the present finding. This consistency suggests that the size-dependent relation $(H/12.6)^{-0.55}$ used for $\sigma_s/\Delta T$ is also valid, at least for $Pr \lesssim 50$.

4. Conclusion and outlook

In summary, we have made a detailed experimental study of Pr effects in quasi-2-D RB convection, spanning the Pr range of $11.7 \leqslant Pr \leqslant 650.7$ and the Ra range of $6.0 \times 10^8 \leqslant Ra \leqslant 3.0 \times 10^{10}$. To achieve these parameter ranges, seven kinds of silicone oil with different viscosities and four rectangular convection cells with different sizes were used in the experiments. The major findings of the present study are as below.

(i) The flow patterns visualized by the shadowgraph technique show that there always exists a well-defined LSC for $11.7 \leqslant Pr \leqslant 145.7$. As Pr increases in this range, the number of thermal plumes that pass through the central region of the convection cell continuously decreases, and the LSC is more confined along the periphery of the system. With Pr further increasing to 345.2 and 650.7, the coherent LSC disappears, which is replaced by slender thermal plumes that move up and down in random locations of the entire cell.

(ii) The breakdown of the LSC results in a regime transition in the Re number, manifested by the sharp drop in magnitude and the steep change in Ra–Pr dependence. For the Pr range with a persistent LSC, the Re data can be well represented by a simple power-law relation as $Re \sim Ra^{0.58}Pr^{-0.82}$. This result is in line with the behaviour in 2-D RB convection. On the other hand, the measured $Nu(Ra, Pr)$ relation is found to be $Nu \sim Ra^{0.289}Pr^{-0.02}$ in the $11.7 \leqslant Pr \leqslant 145.7$ range, which is compatible with the finding in the 3-D system.

(iii) The changes in flow dynamics and plume distribution are also reflected by local temperature fluctuations. It is found that the temperature fluctuation in the cell centre decreases monotonically as Pr increases, but that in the region near the sidewall first depends on Pr weakly and then increases significantly with Pr. In contrast to the global properties, the Ra–Pr dependence of local temperature fluctuation could not be described by a simple unified relation. Their Ra-dependent scalings could not be accounted for with existing models, but the Pr dependences for $Pr \lesssim 50$ are consistent with predictions by Grossmann & Lohse (2004).

Given the scarce experimental studies of Pr effects on RB convection, these results undoubtedly enrich our knowledge of the RB system in quasi-2-D geometry, and the collection of data is thorough enough for model testing/development. Finally, we would like to end this paper by remarking on two preliminary findings that deserve more systematic studies in the future. This first one is the regime transition observed at high Pr numbers, which is similar to that in severely confined RB convection. It is interesting to see how this transition occurs and how Pr number influences the RB system without an LSC. To answer these questions, it requires physically machining more and much larger apparatus from the experimental side, so this topic is beyond the scope of the present study and would be more suitable for numerical simulations. The second one is the effect of system size on local flow properties. Although we have acquired the size-dependent relations for the present data empirically, and their validity was supported by the consistency between our data and the flow features as well as the model predictions, the physical origin of size-dependent behaviours remains unsolved. As many engineering applications are based on scaled-down experiments, this non-trivial phenomenon should receive more attention in future studies.

Supplementary movies. Supplementary movies are available at https://doi.org/10.1017/jfm.2021.21.

Acknowledgements. We thank J.-C. He for his help in this study. We are also grateful to J. Aurnou and Y.-C. Xie for their helpful discussions.

Funding. This work was supported by the National Natural Science Foundation of China (Grant Nos. 11702128, 11961160719 and 91752201) and the Department of Science and Technology of Guangdong Province (Grant No. 2019B21203001).

Author ORCIDs.
Shi-Di Huang https://orcid.org/0000-0001-5719-6428.

Appendix

Tables 2–4 summarize all the experimental parameters (Pr, Ra) and the measured results (Re, Nu), as well as the power-law fitting results for these data as shown in the main text.

Pr	Re		Nu		$(\sigma_c/\Delta T)^*$		$(\sigma_s/\Delta T)^*$	
	C_1	α	C_2	γ	C_3	ζ	C_4	ξ
11.7	0.027	0.53 ± 0.02	0.19	0.282 ± 0.003	7.54	-0.32 ± 0.01	0.92	-0.19 ± 0.01
20.5	0.007	0.57 ± 0.01	0.13	0.298 ± 0.002	5.87	-0.31 ± 0.01	0.50	-0.16 ± 0.01
49.3	0.005	0.56 ± 0.01	0.17	0.284 ± 0.003	2.64	-0.29 ± 0.01	0.37	-0.15 ± 0.01
81.6	5.2×10^{-4}	0.63 ± 0.01	0.13	0.296 ± 0.002	1.74	-0.28 ± 0.01	1.00	-0.18 ± 0.01
145.7	5.5×10^{-4}	0.61 ± 0.01	0.25	0.267 ± 0.003	2.86	-0.32 ± 0.02	1.06	-0.18 ± 0.01
345.2	8.4×10^{-6}	0.73 ± 0.03	—	—	—	—	—	—
650.7	5.8×10^{-7}	0.74 ± 0.05	—	—	—	—	—	—

Table 2. The power-law fitting results for $Re = C_1 Ra^{\alpha}$, $Nu = C_2 Ra^{\gamma}$, $(\sigma_c/\Delta T)^* = C_3 Ra^{\zeta}$ and $(\sigma_s/\Delta T)^* = C_4 Ra^{\xi}$ at different Pr.

Ra	Re		Nu	
	C_5	β	C_6	δ
1.0×10^9	1.3×10^4	-0.89 ± 0.07	68.9	-0.03 ± 0.02
1.6×10^9	1.5×10^4	-0.84 ± 0.07	79.6	-0.03 ± 0.01
2.3×10^9	2.0×10^4	-0.85 ± 0.04	83.6	-0.01 ± 0.01
3.6×10^9	2.7×10^4	-0.85 ± 0.04	93.6	-0.01 ± 0.01
5.9×10^9	2.9×10^4	-0.80 ± 0.05	107.0	-0.010 ± 0.006
9.0×10^9	3.7×10^4	-0.81 ± 0.04	122.9	-0.014 ± 0.002
1.4×10^{10}	4.2×10^4	-0.77 ± 0.05	142.4	-0.020 ± 0.001
2.1×10^{10}	5.0×10^4	-0.76 ± 0.03	161.2	-0.019 ± 0.002

Table 3. The power-law fitting results for $Re = C_5 Pr^{\beta}$ and $Nu = C_6 Pr^{\delta}$ at different Ra.

Pr	*s*/*L*	*Ra*	*Re*	*Nu*	*Pr*	*s*/*L*	*Ra*	*Re*	Nu
11.7	0.102	6.7×10^8	1237.8	63.4	81.6	0.070	1.0×10^9	225.0	60.7
	0.091	9.7×10^8	1540.1	66.2		0.063	1.6×10^9	318.6	68.8
	0.082	1.5×10^9	1752.6	74.4		0.057	2.3×10^9	438.5	77.0
	0.072	2.3×10^9	2545.0	82.3		0.053	3.6×10^9	563.6	88.1
	0.065	3.5×10^9	3106.4	91.9		0.048	5.9×10^9	764.1	101.0
	0.053	5.6×10^9	3808.6	105.4		0.039	9.0×10^9	953.4	115.4
	0.046	8.7×10^9	4982.8	119.3		0.029	1.4×10^{10}	1303.9	130.5
	0.032	1.3×10^{10}	6028.1	135.7		0.022	2.1×10^{10}	1659.5	148.7
	0.024	2.1×10^{10}	7358.0	153.5		0.014	2.7×10^{10}	1789.7	159.7
20.5	0.097	6.7×10^8	725.6	55.7	145.7	0.095	1.0×10^9	175.1	67.7
	0.078	1.0×10^9	885.8	61.7		0.084	1.6×10^9	224.5	74.5
	0.066	1.6×10^9	1217.9	70.4		0.075	2.3×10^9	308.9	80.5
	0.051	2.4×10^9	1663.4	78.8		0.067	3.6×10^9	380.9	89.8
	0.029	3.6×10^9	2006.3	89.2		0.057	5.9×10^9	535.2	103.0
	0.023	5.9×10^9	2623.0	103.5		0.048	9.0×10^9	689.2	115.1
	0.068	2.4×10^9	1527.5	80.0		0.036	1.4×10^{10}	880.6	128.7
	0.057	3.6×10^9	1981.6	90.1		0.025	2.1×10^{10}	1108.8	145.4
	0.044	5.7×10^9	2641.2	103.0	345.2	0.072	1.5×10^9	42.4	—
	0.035	8.8×10^9	3300.8	117.4		0.061	2.3×10^9	65.4	—
	0.024	1.4×10^{10}	4077.7	133.8		0.052	3.5×10^9	85.5	—
	0.018	2.1×10^{10}	5103.7	151.5		0.043	5.7×10^9	121.2	—
	0.015	3.0×10^{10}	6148.9	172.3		0.031	8.7×10^9	172.7	—
49.3	0.082	6.0×10^8	413.2	54.8		0.023	1.4×10^{10}	212.5	—
	0.075	9.8×10^8	480.4	62.2	650.7	0.066	6.7×10^8	1.9	—
	0.069	1.6×10^9	664.6	70.7		0.055	9.7×10^8	2.8	—
	0.066	2.3×10^9	787.4	78.3		0.041	1.6×10^9	4.0	—
	0.054	3.7×10^9	1062.5	89.5		0.032	2.3×10^9	5.0	—
	0.046	5.9×10^9	1429.9	102.6		0.024	3.5×10^9	6.6	—
	0.037	9.1×10^9	1733.7	116.5					
	0.031	1.4×10^{10}	2382.9	132.4					
	0.020	2.1×10^{10}	2781.3	150.3					

Table 4. Experimental parameters (*Pr*, *Ra*) and the measured results (*Re*, *Nu*) for all the measurements in the present study. The positions of the two thermistors T_2 and T_3, i.e. their distance away from the sidewall relative to the cell's length *s*/*L*, are also provided.

References

Ahlers, G., Brown, E., Fontenele Araujo, F., Funfschilling, D., Grossmann, S. & Lohse, D. 2006 Non-Oberbeck–Boussinesq effects in strongly turbulent Rayleigh–Bénard convection. *J. Fluid Mech.* **569**, 409–445.

Ahlers, G., Grossmann, S. & Lohse, D. 2009 Heat transfer and large scale dynamics in turbulent Rayleigh–Bénard convection. *Rev. Mod. Phys.* **81**, 503–537.

Ahlers, G. & Xu, X. 2001 Prandtl-number dependence of heat transport in turbulent Rayleigh–Bénard convection. *Phys. Rev. Lett.* **86**, 3320.

Bakhuis, D., Ostilla-Mónico, R., van der Poel, E.P., Verzicco, R. & Lohse, D. 2018 Mixed insulating and conducting thermal boundary conditions in Rayleigh–Bénard convection. *J. Fluid Mech.* **835**, 491–511.

Bao, Y., Chen, J., Liu, B.-F., She, Z.-S., Zhang, J. & Zhou, Q. 2015 Enhanced heat transport in partitioned thermal convection. *J. Fluid Mech.* **784**, R5.

BELKADI, M., GUISLAIN, L., SERGENT, A., PODVIN, B., CHILLÀ, F. & SALORT, J. 2020 Experimental and numerical shadowgraph in turbulent Rayleigh–Bénard convection with a rough boundary: investigation of plumes. *J. Fluid Mech.* **895**, A7.

BREUER, M, WESSLING, S, SCHMALZL, J & HANSEN, U 2004 Effect of inertia in Rayleigh–Bénard convection. *Phys. Rev.* E **69**, 026302.

BROWN, E., FUNFSCHILLING, D. & AHLERS, G. 2007 Anomalous Reynolds-number scaling in turbulent Rayleigh–Bénard convection. *J. Stat. Mech.* **2007**, P10005.

CASTAING, B., GUNARATNE, G., HESLOT, F., KADANOFF, L., LIBCHABER, A., THOMAE, S., WU, X.-Z., ZALESKI, S. & ZANETTI, G. 1989 Scaling of hard thermal turbulence in Rayleigh–Bénard convection. *J. Fluid Mech.* **204**, 1–30.

CHAVANNE, X., CHILLÀ, F., CHABAUD, B., CASTAING, B. & HÉBRAL, B. 2001 Turbulent Rayleigh–Bénard convection in gaseous and liquid He. *Phys. Fluids* **13**, 1300–1320.

CHEN, J., BAO, Y., YIN, Z.X. & SHE, Z.-S. 2017 Theoretical and numerical study of enhanced heat transfer in partitioned thermal convection. *Intl J. Heat Mass Transfer* **115**, 556–569.

CHEN, X., HUANG, S.-D., XIA, K.-Q. & XI, H.-D. 2019 Emergence of substructures inside the large-scale circulation induces transition in flow reversals in turbulent thermal convection. *J. Fluid Mech.* **877**, R1.

CHILLÀ, F. & SCHUMACHER, J. 2012 New perspectives in turbulent Rayleigh–Bénard convection. *Eur. Phys. J.* E **35**, 58.

CHONG, K.L., HUANG, S.-D., KACZOROWSKI, M. & XIA, K.-Q. 2015 Condensation of coherent structures in turbulent flows. *Phys. Rev. Lett.* **115**, 264503.

CHONG, K.L., WAGNER, S., KACZOROWSKI, M., SHISHKINA, O. & XIA, K.-Q. 2018 Effect of Prandtl number on heat transport enhancement in Rayleigh–Bénard convection under geometrical confinement. *Phys. Rev. Fluids* **3**, 013501.

CHONG, K.L. & XIA, K.-Q. 2016 Exploring the severely confined regime in Rayleigh–Bénard convection. *J. Fluid Mech.* **805**, R4.

DAYA, Z.A. & ECKE, R.E. 2001 Does turbulent convection feel the shape of the container? *Phys. Rev. Lett.* **87**, 184501.

DAYA, Z.A. & ECKE, R.E. 2002 Prandtl-number dependence of interior temperature and velocity fluctuations in turbulent convection. *Phys. Rev.* E **66**, 045301.

EMRAN, M.S. & SHISHKINA, O. 2020 Natural convection in cylindrical containers with isothermal ring-shaped obstacles. *J. Fluid Mech.* **882**, A3.

FOROOZANI, N., NIEMELA, J.J., ARMENIO, V. & SREENIVASAN, K.R. 2019 Turbulent convection and large scale circulation in a cube with rough horizontal surfaces. *Phys. Rev.* E **99**, 033116.

GLOBE, S. & DROPKIN, D. 1959 Natural-convection heat transfer in liquids confined by two horizontal plates and heated from below. *Trans. ASME: J. Heat Transfer* **81**, 24–28.

GROSSMANN, S. & LOHSE, D. 2000 Scaling in thermal convection: a unifying theory. *J. Fluid Mech.* **407**, 27–56.

GROSSMANN, S. & LOHSE, D. 2001 Thermal convection for large Prandtl numbers. *Phys. Rev. Lett.* **86**, 3316.

GROSSMANN, S. & LOHSE, D. 2002 Prandtl and Rayleigh number dependence of the Reynolds number in turbulent thermal convection. *Phys. Rev.* E **66**, 016305.

GROSSMANN, S. & LOHSE, D. 2004 Fluctuations in turbulent Rayleigh–Bénard convection: the role of plumes. *Phys. Fluids* **16**, 4462–4472.

GUO, S.-X., ZHOU, S.-Q., CEN, X.-R., QU, L., LU, Y.-Z., SUN, L. & SHANG, X.-D. 2015 The effect of cell tilting on turbulent thermal convection in a rectangular cell. *J. Fluid Mech.* **762**, 273–287.

HE, G.-W. & ZHANG, J.-B. 2006 Elliptic model for space-time correlations in turbulent shear flows. *Phys. Rev.* E **73**, 055303.

HE, J.-C., FANG, M.-W., GAO, Z.-Y., HUANG, S.-D. & BAO, Y. 2021 Effects of Prandtl number in two-dimentional turbulent convection. *Chin. Phys.* B (submitted).

HE, X., HE, G.-W. & TONG, P. 2010 Small-scale turbulent fluctuations beyond Taylor's frozen-flow hypothesis. *Phys. Rev.* E **81**, 065303.

HUANG, S.-D., KACZOROWSKI, M., NI, R. & XIA, K.-Q. 2013 Confinement-induced heat-transport enhancement in turbulent thermal convection. *Phys. Rev. Lett.* **111**, 104501.

HUANG, S.-D., WANG, F., XI, H.-D. & XIA, K.-Q. 2015 Comparative experimental study of fixed temperature and fixed heat flux boundary conditions in turbulent thermal convection. *Phys. Rev. Lett.* **115**, 154502.

HUANG, S.-D. & XIA, K.-Q. 2016 Effects of geometric confinement in quasi-2-D turbulent Rayleigh–Bénard convection. *J. Fluid Mech.* **794**, 639–654.

HUANG, Y.-X. & ZHOU, Q. 2013 Counter-gradient heat transport in two-dimensional turbulent Rayleigh–Bénard convection. *J. Fluid Mech.* **737**, R3.

JIANG, L., SUN, C. & CALZAVARINI, E. 2019 Robustness of heat transfer in confined inclined convection at high Prandtl number. *Phys. Rev.* E **99**, 013108.

KERR, R.M. & HERRING, J.R. 2000 Prandtl number dependence of Nusselt number in direct numerical simulations. *J. Fluid Mech.* **419**, 325–344.

KRAICHNAN, R.H. 1962 Turbulent thermal convection at arbitrary Prandtl number. *Phys. Fluids* **5**, 1374–1389.

LAKKARAJU, R., STEVENS, R.J.A.M., VERZICCO, R., GROSSMANN, S., PROSPERETTI, A., SUN, C. & LOHSE, D. 2012 Spatial distribution of heat flux and fluctuations in turbulent Rayleigh-Bénard convection. *Phys. Rev.* E **86**, 056315.

LAM, S., SHANG, X.-D., ZHOU, S.-Q. & XIA, K.-Q. 2002 Prandtl number dependence of the viscous boundary layer and the Reynolds numbers in Rayleigh–Bénard convection. *Phys. Rev.* E **65**, 066306.

LIU, S., JIANG, L., CHONG, K.L., ZHU, X., WAN, Z.-H., VERZICCO, R., STEVENS, R.J.A.M., LOHSE, D. & SUN, C. 2020 From Rayleigh–Bénard convection to porous-media convection: how porosity affects heat transfer and flow structure. *J. Fluid Mech.* **895**, A18.

LOHSE, D. & XIA, K.-Q. 2010 Small-scale properties of turbulent Rayleigh–Bénard convection. *Annu. Rev. Fluid Mech.* **42**, 335–364.

MUSILOVÁ, V., KRÁLIK, T., LA MANTIA, M., MACEK, M., URBAN, P. & SKRBEK, L. 2017 Reynolds number scaling in cryogenic turbulent Rayleigh–Bénard convection in a cylindrical aspect ratio one cell. *J. Fluid Mech.* **832**, 721–744.

NI, R., HUANG, S.-D. & XIA, K.-Q. 2011*a* Local energy dissipation rate balances local heat flux in the center of turbulent thermal convection. *Phys. Rev. Lett.* **107**, 174503.

NI, R., ZHOU, S.-Q. & XIA, K.-Q. 2011*b* An experimental investigation of turbulent thermal convection in water-based alumina nanofluid. *Phys. Fluids* **23**, 022005.

NIEMELA, J.J. & SREENIVASAN, K.R. 2003 Rayleigh-number evolution of large-scale coherent motion in turbulent convection. *Europhys. Lett.* **62**, 829–833.

PANDEY, A., VERMA, M.K., CHATTERJEE, A.G. & DUTTA, B. 2016 Similarities between 2D and 3D convection for large Prandtl number. *Pramana-J. Phys.* **87**, 13.

VAN DER POEL, E.P., STEVENS, R.J.A.M. & LOHSE, D. 2013 Comparison between two- and three-dimensional Rayleigh–Bénard convection. *J. Fluid Mech.* **736**, 177–194.

VAN DER POEL, E.P., STEVENS, R.J.A.M., SUGIYAMA, K. & LOHSE, D. 2012 Flow states in two-dimensional Rayleigh–Bénard convection as a function of aspect-ratio and Rayleigh number. *Phys. Fluids* **24**, 085104.

RIPESI, P., BIFERALE, L., SBRAGAGLIA, M. & WIRTH, A. 2014 Natural convection with mixed insulating and conducting boundary conditions: low- and high-Rayleigh-number regimes. *J. Fluid Mech.* **742**, 636–663.

ROCHE, P.-E., CASTAING, B., CHABAUD, B. & HÉBRAL, B. 2002 Prandtl and Rayleigh numbers dependences in Rayleigh–Bénard convection. *Europhys. Lett.* **58**, 693.

RUSAOUËN, E., LIOT, O., CASTAING, B., SALORT, J. & CHILLÀ, F. 2018 Thermal transfer in Rayleigh–Bénard cell with smooth or rough boundaries. *J. Fluid Mech.* **837**, 443–460.

SCHMALZL, J., BREUER, M. & HANSEN, U. 2004 On the validity of two-dimensional numerical approaches to time-dependent thermal convection. *Europhys. Lett.* **67**, 390.

SHANG, X.-D., TONG, P. & XIA, K.-Q. 2008 Scaling of the local convective heat flux in turbulent Rayleigh–Bénard convection. *Phys. Rev. Lett.* **100**, 244503.

SHISHKINA, O., EMRAN, M.S., GROSSMANN, S. & LOHSE, D. 2017 Scaling relations in large-Prandtl-number natural thermal convection. *Phys. Rev. Fluids* **2**, 103502.

SHISHKINA, O. & HORN, S. 2016 Thermal convection in inclined cylindrical containers. *J. Fluid Mech.* **790**, R3.

SHRAIMAN, B.I. & SIGGIA, E.D. 1990 Heat transport in high-Rayleigh-number convection. *Phys. Rev.* A **42**, 3650–3653.

SILANO, G., SREENIVASAN, K.R. & VERZICCO, R. 2010 Numerical simulations of Rayleigh–Bénard convection for Prandtl numbers between 10^{-1} and 10^{4} and Rayleigh numbers between 10^{5} and 10^{9}. *J. Fluid Mech.* **662**, 409–446.

STEVENS, R.J.A.M., LOHSE, D. & VERZICCO, R. 2011 Prandtl and Rayleigh number dependence of heat transport in high Rayleigh number thermal convection. *J. Fluid Mech.* **688**, 31–43.

STEVENS, R.J.A.M., VAN DER POEL, E.P, GROSSMANN, S. & LOHSE, D. 2013 The unifying theory of scaling in thermal convection: the updated prefactors. *J. Fluid Mech.* **730**, 295–308.

SUGIYAMA, K., CALZAVARINI, E., GROSSMANN, S. & LOHSE, D. 2009 Flow organization in two-dimensional non-Oberbeck–Boussinesq Rayleigh–Bénard convection in water. *J. Fluid Mech.* **637**, 105–135.

SUGIYAMA, K., NI, R., STEVENS, R.J.A.M., CHAN, T.S., ZHOU, S.-Q., XI, H.-D., SUN, C., GROSSMANN, S., XIA, K.-Q. & LOHSE, D. 2010 Flow reversals in thermally driven turbulence. *Phys. Rev. Lett.* **105**, 034503.

TOPPALADODDI, S., SUCCI, S. & WETTLAUFER, J.S. 2017 Roughness as a route to the ultimate regime of thermal convection. *Phys. Rev. Lett.* **118**, 074503.

VERZICCO, R. & CAMUSSI, R. 1999 Prandtl number effects in convective turbulence. *J. Fluid Mech.* **383**, 55–73.

WAGNER, S. & SHISHKINA, O. 2013 Aspect-ratio dependency of Rayleigh–Bénard convection in box-shaped containers. *Phys. Fluids* **25**, 085110.

WAGNER, S. & SHISHKINA, O. 2015 Heat flux enhancement by regular surface roughness in turbulent thermal convection. *J. Fluid Mech.* **763**, 109–135.

WANG, B.-F., ZHOU, Q. & SUN, C. 2020*a* Vibration-induced boundary-layer destabilization achieves massive heat-transport enhancement. *Sci. Adv.* **6**, eaaz8239.

WANG, F., HUANG, S.-D. & XIA, K.-Q. 2017 Thermal convection with mixed thermal boundary conditions: effects of insulating lids at the top. *J. Fluid Mech.* **817**, R1.

WANG, F., HUANG, S.-D., ZHOU, S.-Q. & XIA, K.-Q. 2016 Laboratory simulation of the geothermal heating effects on ocean overturning circulation. *J. Geophys. Res.: Oceans* **121**, 7589–7598.

WANG, Q., CHONG, K.L., STEVENS, R.J.A.M., VERZICCO, R. & LOHSE, D. 2020*b* From zonal flow to convection rolls in Rayleigh–Bénard convection with free-slip plates. *J. Fluid Mech.* **905**, A21.

WANG, Q., XIA, S.-N., WANG, B.-F., SUN, D.-J., ZHOU, Q. & WAN, Z.-H. 2018 Flow reversals in two-dimensional thermal convection in tilted cells. *J. Fluid Mech.* **849**, 355–372.

WEI, P., NI, R. & XIA, K.-Q. 2012 Enhanced and reduced heat transport in turbulent thermal convection with polymer additives. *Phys. Rev.* E **86**, 016325.

WEN, B., GOLUSKIN, D., LEDUC, M., CHINI, G.P. & DOERING, C.R. 2020 Steady Rayleigh–Bénard convection between stress-free boundaries. *J. Fluid Mech.* **905**, R4.

WU, X.-Z. & LIBCHABER, A. 1991 Non-Boussinesq effects in free thermal convection. *Phys. Rev.* A **43**, 2833–2839.

WUNSCH, S. & KERSTEIN, A.R 2005 A stochastic model for high-Rayleigh-number convection. *J. Fluid Mech.* **528**, 173–205.

XI, H.-D., LAM, S. & XIA, K.-Q. 2004 From laminar plumes to organized flows: the onset of large-scale circulation in turbulent thermal convection. *J. Fluid Mech.* **503**, 47–56.

XI, H.-D. & XIA, K.-Q. 2008 Azimuthal motion, reorientation, cessation, and reversal of the large-scale circulation in turbulent thermal convection: a comparative study in aspect ratio one and one-half geometries. *Phys. Rev.* E **78**, 036326.

XIA, K.-Q., LAM, S. & ZHOU, S.-Q. 2002 Heat-flux measurement in high-Prandtl-number turbulent Rayleigh–Bénard convection. *Phys. Rev. Lett.* **88**, 064501.

XIA, K.-Q., SUN, C. & ZHOU, S.-Q. 2003 Particle image velocimetry measurement of the velocity field in turbulent thermal convection. *Phys. Rev.* E **68**, 066303.

XIE, Y.-C., CHENG, B.-Y.-C., HU, Y.-B. & XIA, K.-Q. 2019 Universal fluctuations in the bulk of Rayleigh–Bénard turbulence. *J. Fluid Mech.* **878**, R1.

XIE, Y.-C. & XIA, K.-Q. 2017 Turbulent thermal convection over rough plates with varying roughness geometries. *J. Fluid Mech.* **825**, 573–599.

YANG, R., CHONG, K.L., WANG, Q., VERZICCO, R., SHISHKINA, O. & LOHSE, D. 2020*a* Periodically modulated thermal convection. *Phys. Rev. Lett.* **125**, 154502.

YANG, Y.-H., ZHU, X., WANG, B.-F., LIU, Y.-L. & ZHOU, Q. 2020*b* Experimental investigation of turbulent Rayleigh–Bénard convection of water in a cylindrical cell: the Prandtl number effects for $Pr > 1$. *Phys. Fluids* **32**, 015101.

ZHANG, J., CHILDRESS, S. & LIBCHABER, A. 1997 Non-Boussinesq effect: thermal convection with broken symmetry. *Phys. Fluids* **9**, 1034–1042.

ZHANG, Y., ZHOU, Q. & SUN, C. 2017 Statistics of kinetic and thermal energy dissipation rates in two-dimensional turbulent Rayleigh–Bénard convection. *J. Fluid Mech.* **814**, 165–184.

ZHANG, Y.-Z., SUN, C., BAO, Y. & ZHOU, Q. 2018 How surface roughness reduces heat transport for small roughness heights in turbulent Rayleigh–Bénard convection. *J. Fluid Mech.* **836**, R2.

ZHOU, Q., LIU, B.-F., LI, C.-M. & ZHONG, B.-C. 2012 Aspect ratio dependence of heat transport by turbulent Rayleigh–Bénard convection in rectangular cells. *J. Fluid Mech.* **710**, 260–276.

ZHU, X., STEVENS, R.J.A.M., SHISHKINA, O., VERZICCO, R. & LOHSE, D. 2019 $Nu \sim Ra^{1/2}$ scaling enabled by multiscale wall roughness in Rayleigh–Bénard turbulence. *J. Fluid Mech.* **869**, R4.

ZWIRNER, L., KHALILOV, R., KOLESNICHENKO, I., MAMYKIN, A., MANDRYKIN, S., PAVLINOV, A., SHESTAKOV, A., TEIMURAZOV, A., FRICK, P. & SHISHKINA, O. 2020 The influence of the cell inclination on the heat transport and large-scale circulation in liquid metal convection. *J. Fluid Mech.* **884**, A18.